Mean Body Initial Condition Implementation in the EIT Reconstruction Problem

Chris Rocheleau

Department of Mathematics, Colorado State University

Abstract—**Electrical Impedance Tomography (EIT) is a non-ionizing technology for imaging of a patient's internal body structure and functions from administration of currents and measuring the resulting voltages at electrodes across the body's surface and solving an inverse problem to estimate the electrical properties of the body. Among the existing methods, the NOSER[2] algorithm reconstructs cross-sectional images in real-time using one step of a Newton-Gauss solver aiming to minimize the sum of the squared differences between estimated and actual voltage measurements using a constant conductivity model as an initial guess. Using an Anatomical Atlas of 89 infants, we create an estimate of a mean chest cavity and its corresponding effect on the estimated voltage measurements. This allows us to use a more accurate initial condition than is used in NOSER while maintaining the speed benefits of performing a single Gauss-Newton method step, resulting in more detailed images while maintaining real-time implementation. We will compare reconstructed images using each algorithm on simulated and experimentally measured voltages and explore a Schur complement-based post-processing technique for further improved resolution.**

I. Electrical Impedence Tomography

Electrical Impedence Tomography (EIT) is a non-ionizing real-time method for imaging internal body structures and functions using electrical properties. By administering a low-amplitude current to electrodes on the body surface and measuring resulting voltages, one can solve an inverse problem for the electrical conductivity and permittivity distributions throughout the body. As, especially in the chest, there is a broad range of conductivity values for different components of the body, this allows the user to visualize the distributions spatially and interpret the values as a representation of the body.

For example, comparison of the conductivity of heart tissue (approximately 0.5 S/m when full of blood) and lung tissue (0.15 S/m during full inspiration) to its surrounding soft tissue with conductivity around 0.3 S/m, creates a contrast that makes EIT effective in visualization of cardiopulmonary imaging. This, coupled with real-time processing and portable form factor, makes EIT an attractive option for bedside monitoring of patients with pulmonary issues.

A. Mathematical Formulation

To develop a mathematical model we will denote the L electrodes placed on the surface of the body as e_l for $l = 1, \ldots, L$, and the corresponding currents applied to the electrodes as I_l.

We will consider $(L-1)$ linearly independent current patterns I_l^k such that $\sum_{l=1}^{L} I_l^k = 0$. For convenience of calculations we will focus on trigonometric patterns defined as

$$I_l^k = T_l^k = \begin{cases} \cos(k\theta_l), & k = 1, \ldots, L/2 \\ \sin((k - L/2)\theta_l), & k = L/2 + 1, \ldots, L - 1 \end{cases} \tag{1}$$

where $\theta_l = \frac{2\pi l}{L}$ represents the angle from a reference point in the body to the lth electrode. Since this constitutes a basis for current patterns, any other set of currents patterns may be rewritten as a linear combination of these trigonometric patterns.

It is shown in [8], that the partial differential equations that describe the electric potential u at a point $\boldsymbol{p}$ in a 2-dimensional cross-section of a body B from a current density $j(\boldsymbol{p})$ applied at the body surface S are

$$\nabla \cdot \sigma \nabla u(\boldsymbol{p}) = 0 \qquad \text{for } \boldsymbol{p} \text{ in } B \tag{2}$$

$$\sigma(\boldsymbol{p})\frac{\partial u(\boldsymbol{p})}{\partial \nu} = j(\boldsymbol{p}) \qquad \text{for } \boldsymbol{p} \text{ on } S \tag{3}$$

where σ represents our conductivity distribution and ν is the outward normal vector to the body surface. Our inverse problem thus becomes, given applied currents T_l^k and voltages V_l^k needed to maintain the current pattern for each electrode $l = 1, \ldots, L$ and current pattern $k = 1, \ldots, L-1$ to determine the conductivity distribution σ of the body B.

II. NOSER Reconstruction Algorithm

One of the most commonly used algorithms to determine a solution to the inverse problem is the Newton's One-Step Error Reconstructor, commonly known as NOSER [2]. This algorithm aims to find an approximation for the true conductivity distribution that minimizes the square error between estimated output voltages and the experimental voltage measurements through using a Newton-Gauss solver. However, the components needed for such algorithm are computationally expensive and only a single iteration is performed.

A. Least-Squares Approach

In order to simplify the solution process, the NOSER algorithm seeks to find a conductivity distribution that minimizes the errors $\boldsymbol{V}^k - \boldsymbol{U}^k(\boldsymbol{\sigma})$ in the least-squares sense, where $\boldsymbol{V}^1, \ldots, \boldsymbol{V}^{L-1}$ represent the measured voltages for each of the $L-1$ current patterns and $\boldsymbol{U}^1(\boldsymbol{\sigma}), \ldots, \boldsymbol{U}^{L-1}(\boldsymbol{\sigma})$ are the corresponding estimated voltages assuming a conductivity distribution $\boldsymbol{\sigma}$. Additionally, in order to simplify later equations,

NOSER utilized the resistivity distribution, $\boldsymbol{\rho}$, which is the reciprocal of conductivity. The error functional is given by

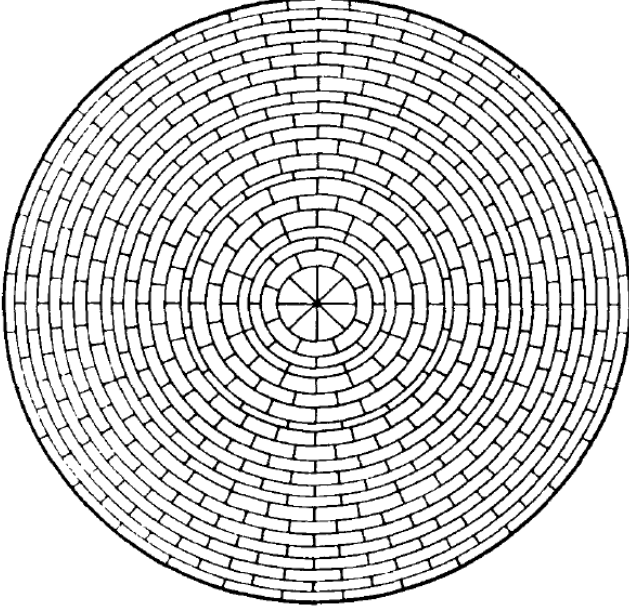$$E(\boldsymbol{\rho}) = \sum_{k=1}^{L-1} \sum_{l=1}^{L} (V_l^k - U_l^k(\boldsymbol{\rho}))^2 \qquad (4)$$

Fig. 1. 496 elements of the Joshua tree mesh used in NOSER reconstructions.

Reconstructions are computed on the $N = 496$ element Joshua tree mesh shown in Figure 1, with resistivity — and conductivity as well — assumed to be constant within each elements of the mesh. To find the necessary conditions for minimization of the error functional, we differentiate with respect to each point $\rho_1, \ldots, \rho_N$ in our conductivity distribution and find the system of N equations that must be satisfied

$$0 = \frac{\partial E(\boldsymbol{\rho})}{\partial \rho_n} = -2 \sum_{k=1}^{L-1} \sum_{l=1}^{L} (V_l^k - U_l^k(\boldsymbol{\rho})) \frac{\partial U_l^k(\boldsymbol{\rho})}{\partial \rho_n} \qquad (5)$$

Now that we are left with a system of nonlinear equations, the Gauss-Newton method is used as a standard method for approximating a solution. Given an initial resistivity guess $\tilde{\boldsymbol{\rho}}$ we compute an update $\hat{\boldsymbol{\rho}}$ using the following algorithm

$$\hat{\boldsymbol{\rho}} = \tilde{\boldsymbol{\rho}} - [\boldsymbol{F}'(\tilde{\boldsymbol{\rho}})]^{-1} \boldsymbol{F}(\tilde{\boldsymbol{\rho}}) \qquad (6)$$

$$F_n(\tilde{\boldsymbol{\rho}}) = -2 \sum_{k=1}^{L-1} \sum_{l=1}^{L} (V_l^k - U_l^k(\tilde{\boldsymbol{\rho}})) \frac{\partial U_l^k(\tilde{\boldsymbol{\rho}})}{\partial \rho_n} \qquad (7)$$

$$F'_{n,m}(\tilde{\boldsymbol{\rho}}) \approx 2 \sum_{k=1}^{L-1} \sum_{l=1}^{L} \frac{\partial U_l^k(\tilde{\boldsymbol{\rho}})}{\partial \rho_n} \frac{\partial U_l^k(\tilde{\boldsymbol{\rho}})}{\partial \rho_m} \qquad (8)$$

Where second-order derivative terms are excluded from $F'_{n,m}(\tilde{\boldsymbol{\rho}})$, as they are assumed to be expensive to compute and

relatively small in comparison to the first order terms listed in equation 8.

As we will see, every iteration requires finding estimates for each $U_l^k(\tilde{\boldsymbol{\rho}})$ and $\frac{\partial U_l^k(\tilde{\boldsymbol{\rho}})}{\partial \rho_n}$. This process requires some assumptions to be made for simplification purposes. As these assumptions can only be guaranteed for the first iteration, NOSER only performs the first step of the Netwon-Gauss method and uses the reciprocal of the resulting resistivities as the reconstruction solution. In practice, in order to address the ill-posed nature of inverting $\boldsymbol{F}'(\tilde{\boldsymbol{\rho}})$, an approximation using Levenberg-Marquardt regularization is used in place of $\boldsymbol{F}'(\tilde{\boldsymbol{\rho}})$ to force it to be diagonally dominant. Thus for regularization parameter γ we use $F'_{n,m} + \gamma F'_{n,m} \delta_{n,m}$, where $\delta_{n,m}$ is the Kronecker delta function. For the reconstructions used in this paper, $\gamma = 25$ was used for synthetic data and $\gamma = 4.5$ used for experimental data.

B. Numerical Simplifications

To simplify computations, NOSER assumes a constant conductivity (and thus resistivity as well) initial condition $\tilde{\boldsymbol{\rho}} = \rho_b \mathbf{1}$, where ρ_b is the constant resistivity value that fits best to the measured data in the least squares sense. Since the partial differential equation 2 is linear with respect to $\boldsymbol{\rho}$, we can rewrite $U_l^k(\tilde{\boldsymbol{\rho}}) = \rho_b U_l^k(\mathbf{1})$. Thus we want to find ρ_b that minimizes $E(\rho_b) = \sum_{k=1}^{L-1} \sum_{l=1}^{L} (V_l^k - \rho_b U_l^k(\mathbf{1}))^2$. Which we differentiate and solve for the critical point ρ_b below.

$$\rho_b = \frac{\sum_{k=1}^{L-1} \sum_{l=1}^{L} V_l^k U_l^k(\mathbf{1})}{\sum_{k=1}^{L-1} \sum_{l=1}^{L} [U_l^k(\mathbf{1})]^2} \qquad (9)$$

Additionally, for a constant resistivity profile, equations 2 and 3 can be solved for application of trigonometric current patterns on the boundary. Letting voltage $U_l^k(\mathbf{1})$ be the potential at the center of each electrode

$$U_l^k(\mathbf{1}) = \begin{cases} \frac{r_0}{k} T_l^k, & k = 1, \ldots, L/2 \\ \frac{r_0}{k - L/2} T_l^k, & k = L/2 + 1, \ldots, L \end{cases} \qquad (10)$$

where T_l^k are given in 1. This allows us to compute ρ_b and $U_l^k(\tilde{\boldsymbol{\rho}})$. The final piece needed to compute $\boldsymbol{F}(\tilde{\boldsymbol{\rho}})$ and $\boldsymbol{F}'(\tilde{\boldsymbol{\rho}})$ is to find $\frac{\partial U_l^k(\tilde{\boldsymbol{\rho}})}{\partial \rho_n}$. This is done by breaking each vector $\frac{\partial \boldsymbol{U}^k(\tilde{\boldsymbol{\rho}})}{\partial \rho_n}$ into a sum of components of the trigonometric bases and computed by

$$\frac{\partial \boldsymbol{U}^k(\tilde{\boldsymbol{\rho}})}{\partial \rho_n} = \rho_b \frac{\partial \boldsymbol{U}^k(\mathbf{1})}{\partial \rho_n} = \rho_b \sum_{s=1}^{L-1} \frac{\left\langle \boldsymbol{T}^s, \frac{\partial \boldsymbol{U}^k(\mathbf{1})}{\partial \rho_n} \right\rangle}{\langle \boldsymbol{T}^s, \boldsymbol{T}^s \rangle} \qquad (11)$$

where we can compute the inner products needed in 11 on the given mesh where M_n represents the nth mesh element.

$$\langle \boldsymbol{T}^s, \boldsymbol{T}^s \rangle = \begin{cases} L/2, & s = 1, \ldots, L/2 \\ L, & s = L/2 + 1, \ldots, L \end{cases} \qquad (12)$$

$$\left\langle \boldsymbol{T}^s, \frac{\partial \boldsymbol{U}^k(\mathbf{1})}{\partial \rho_n} \right\rangle = \int_{M_n} \left(\frac{\partial u^k}{\partial r} \frac{\partial u^s}{\partial r} + \frac{1}{r^2} \frac{\partial u^k}{\partial \theta} \frac{\partial u^s}{\partial \theta} \right) \qquad (13)$$

These gradients can be computed ahead of time, so in practice only ρ_b and $\boldsymbol{F}(\rho_b\mathbf{1})$ need to be computed separately for each measurement to find $\hat{\boldsymbol{\rho}}$, allowing the solution to be computed quickly.

III. IMPROVED INITIAL GUESS

Since only one step of the Newton-Gauss method is used in NOSER, we assume applying a more accurate initial condition will result in a more accurate approximation. Additionally, many of the analytical tools used by NOSER are results of the constant resistivity assumption, a computational approach must be used to implement a different initial condition. For our approach, we use an anatomical atlas of cross-sectional images to compute a model of the average conductivity distribution and estimates of corresponding voltages and gradients. An additional benefit of this approach is to keep our formulation in terms of conductivity $\boldsymbol{\sigma}$, so we can rewrite equations 4 and 6 - 8

$$\hat{\boldsymbol{\sigma}} = \tilde{\boldsymbol{\sigma}} - [\boldsymbol{F}'(\tilde{\boldsymbol{\sigma}})]^{-1}\boldsymbol{F}(\tilde{\boldsymbol{\sigma}}) \tag{14}$$

$$F_n(\tilde{\boldsymbol{\sigma}}) = -2\sum_{k=1}^{L-1}\sum_{l=1}^{L}(V_l^k - U_l^k(\tilde{\boldsymbol{\sigma}}))\frac{\partial U_l^k(\tilde{\boldsymbol{\sigma}})}{\partial \sigma_n} \tag{15}$$

$$F_{n,m}'(\tilde{\boldsymbol{\sigma}}) \approx 2\sum_{k=1}^{L-1}\sum_{l=1}^{L}\frac{\partial U_l^k(\tilde{\boldsymbol{\sigma}})}{\partial \sigma_n}\frac{\partial U_l^k(\tilde{\boldsymbol{\sigma}})}{\partial \sigma_m}. \tag{16}$$

The anatomical atlas[4] used in this work is comprised of a set of 8,171 2-D cross-sectional images taken at the chest using CT scans of 89 infants aged 0 to 3 months selected from the New Mexico Decedent Image Database [3]. Each CT scan was then segmented into lung, trachea, heart, bone, and soft tissue using the ITK-SNAP 4.0.0[10] software. Since the windowing of the CT scans did not permit the hearts to be visible, "average" hearts were manually drawn in each slice.

For each slice, a mask was imported into MATLAB R2023a [9] with boundaries around each organ. Conductivity values were prescribed to each type of tissue according to Table I allowing a finite element method solver to be used to numerically compute EIT voltage patterns. As our initial guess will be tailored to the anatomy of infant subjects, EIT modeling is performed in accordance with data collection procedures on infants at Children's Hospital Colorado using the ACT5 system, using $L = 16$ electrodes and 15 trigonometric current patterns.

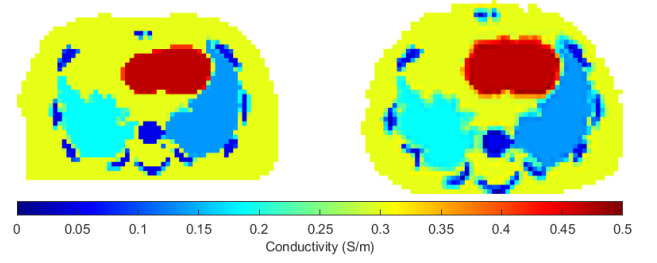### A. Computation of Mean Components

Fig. 2. An example of the conformal mapping of slices from the anatomical atlas to a common body shape for computation of mean.

When computing $\tilde{\boldsymbol{\sigma}} = \bar{\boldsymbol{\sigma}}$ as our initial condition, each slice was remapped to a common body shape using a conformal mapping based on the angle of each pixel from the center of the body and distance relative to the body boundary in that direction, an example of this mapping can be seen in Figure 2. This is intended to mitigate any artifacts that may arise due to the different body shapes and sizes seen in the atlas, putting a primary focus on the internal structures of the body. The mean distribution, $\bar{\boldsymbol{\sigma}}$ is then calculated by taking the mean value for each pixel and shown in Figure 3.
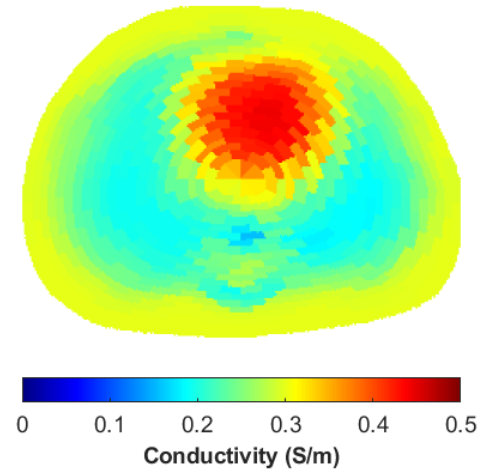

Fig. 3. The average distribution, $\bar{\boldsymbol{\sigma}}$, from the ground truth conductivity distributions in the anatomical atlas.
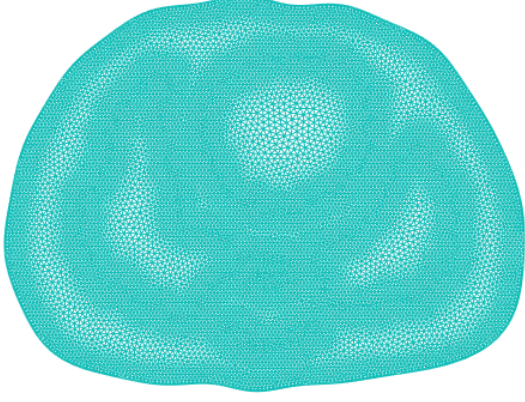
Tissue	Heart	Soft Tissue	Lung	Trachea	Bone
Conductivity base value (S/m)	0.5	0.3	0.15	0.15	0.05
Maximum perturbation (S/m)	± 0.1	± 0	± 0.3	± 0.05	± 0.05

TABLE I
ANATOMICAL ATLAS ASSIGNED CONDUCTIVITY VALUES PER TISSUE AND THEIR MAXIMUM PERTURBATION RANGE.

$$F'_{n,m}(\bar{\boldsymbol{\sigma}}) = \mathbf{A}_{n,m} + \gamma \mathbf{A}_{n,m}\delta_{n,m} \quad (17)$$

$$\boldsymbol{F}' = \boldsymbol{F}' + \alpha \max_n (F'_{n,n})I, \quad (18)$$

where $\mathbf{A}$ is the matrix $\boldsymbol{F}'(\bar{\boldsymbol{\sigma}})$ as determined using (16), $\delta_{n,m}$ is the Kroenecker delta function, and γ and α are regularization parameters to improve the conditioning of $\boldsymbol{F}'$. In this case, the values $\gamma = 10$ and $\alpha = 0.001$ were used, determined empirically. However, in practice the user may alter these parameters as needed for their specific circumstance. Algorithm 1 outlines the steps of the "Mean Baby" method, which has a runtime of 3.3 ms, not including figure rendering.

Algorithm 1: Mean Baby Approach

Input: Measured voltages V, estimated voltages $U(\boldsymbol{\sigma})$ for initial conductivity distribution $\bar{\boldsymbol{\sigma}}$, and corresponding gradients $\frac{\partial U_l^k(\bar{\boldsymbol{\sigma}})}{\partial \sigma_n}$, regularization parameters α and γ.

Result: Reconstructed conductivity distribution $\hat{\boldsymbol{\sigma}}$

1: Let $\tilde{\boldsymbol{\sigma}} = \bar{\boldsymbol{\sigma}}$ and $U(\tilde{\boldsymbol{\sigma}}) = U(\bar{\boldsymbol{\sigma}})$
2: Compute $\boldsymbol{F}(\bar{\boldsymbol{\sigma}})$ and $\boldsymbol{F}'(\bar{\boldsymbol{\sigma}})$ from (15) and (16) – (18)
3: Solve $\hat{\boldsymbol{\sigma}} = \bar{\boldsymbol{\sigma}} - [\boldsymbol{F}'(\bar{\boldsymbol{\sigma}})]^{-1}\boldsymbol{F}(\bar{\boldsymbol{\sigma}})$

Fig. 4. Example meshing used in finite element method voltage estimation.

Once the mean conductivity distribution is calculated, the finite element method solver is used to numerically find an approximation of the voltage pattern $\boldsymbol{U}(\bar{\boldsymbol{\sigma}})$. In order to estimate the gradients $\frac{\partial U_l^k(\bar{\boldsymbol{\sigma}})}{\partial \sigma_n}$ for each σ_n on a Joshua tree mesh conformally mapped to a chest-shaped boundary shown in Figure 5. Each node of the finite element mesh contained in the nth element of the Joshua tree mesh has its conductivity perturbed by $\epsilon = \pm 0.01$ S/m and a central difference estimate of the gradient is calculated using the results of the finite element method. This requires 2N iterations, but the results are stored for future use, allowing the processing speed seen in NOSER to be maintained.
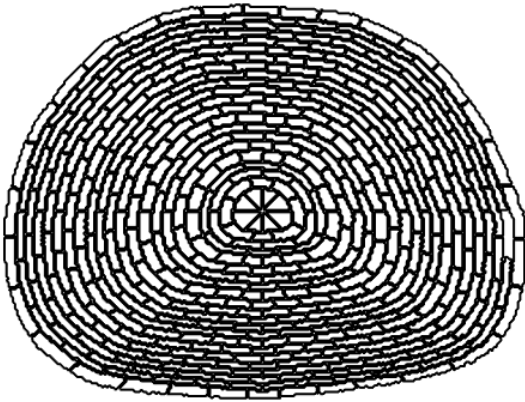

Fig. 5. Remapped Joshua tree mesh used in Mean Baby reconstructions.

Finally, as is also seen in NOSER, our $\boldsymbol{F}'$ matrix is ill-conditioned so we use a combination of Levenberg-Marquardt and Tikhonov regularization. Our Jacobian is then computed using

IV. SCHUR COMPLEMENT POST-PROCESSING

In addition to allowing us to compute and implement a mean initial condition into the NOSER algorithm, the anatomical atlas allows reconstruction images to be post-processed based on prior statistical data as seen in [5] and [6]. Since we have ground truth conductivity distributions $\boldsymbol{\sigma}$ for each image in our anatomical atlas, we can compute a pixel-wise covariance matrix, Γ, of the joint distribution between the ground truth images and their corresponding reconstructions. Interpreting Γ as a block matrix we see

$$\Gamma = \begin{bmatrix} \Gamma_{\boldsymbol{\sigma\sigma}} & \Gamma_{\boldsymbol{\sigma\hat{\sigma}}} \\ \Gamma_{\boldsymbol{\hat{\sigma}\sigma}} & \Gamma_{\boldsymbol{\hat{\sigma}\hat{\sigma}}} \end{bmatrix} \quad (19)$$

where $\Gamma_{\boldsymbol{\sigma\sigma}}$ and $\Gamma_{\boldsymbol{\hat{\sigma}\hat{\sigma}}}$ are the covariance matrices of the ground truth and reconstruction images, respectively, while $\Gamma_{\boldsymbol{\sigma\hat{\sigma}}}$ and $\Gamma_{\boldsymbol{\hat{\sigma}\sigma}}$ are our cross-covariance matrices. Using the Schur complement property for symmetric positive definite matrices we can find the expected value of the true conductivity distribution given a reconstructed image $\hat{\boldsymbol{\sigma}}$.

$$\mathbb{E}(\boldsymbol{\sigma}|\hat{\boldsymbol{\sigma}}) = \bar{\boldsymbol{\sigma}} + \Gamma_{\boldsymbol{\sigma\hat{\sigma}}}\Gamma_{\boldsymbol{\hat{\sigma}\hat{\sigma}}}^{-1}(\hat{\boldsymbol{\sigma}} - \boldsymbol{\mu}_{\hat{\boldsymbol{\sigma}}}) \quad (20)$$

The term $\boldsymbol{\mu}_{\hat{\boldsymbol{\sigma}}}$ is found by taking the mean value of each pixel in our reconstruction image, akin to calculation of $\bar{\boldsymbol{\sigma}}$ from the ground truth images described in Section III-A. In practice, since $\Gamma_{\boldsymbol{\hat{\sigma}\hat{\sigma}}}$ may be ill-conditioned we regularize the matrix using diagonal ridge regression by adding a diagonal term κI using $\kappa = 10^{-5}$. We will use this updated estimate of $\mathbb{E}(\boldsymbol{\sigma}|\hat{\boldsymbol{\sigma}})$ as our Schur complement post-processed reconstruction of the conductivity distribution

$$\hat{\boldsymbol{\sigma}}_S = \bar{\boldsymbol{\sigma}} + \Gamma_{\boldsymbol{\sigma\hat{\sigma}}}(\Gamma_{\boldsymbol{\hat{\sigma}\hat{\sigma}}} + \kappa I)^{-1}(\hat{\boldsymbol{\sigma}} - \boldsymbol{\mu}_{\hat{\boldsymbol{\sigma}}}) \quad (21)$$

For implementation, we recognize that this equation can be rewritten in the form $\hat{\boldsymbol{\sigma}}_S = \boldsymbol{A}_\kappa \hat{\boldsymbol{\sigma}} + \boldsymbol{b}_\kappa$ where we can precompute

$$\boldsymbol{A}_\kappa = \Gamma_{\boldsymbol{\sigma}\hat{\boldsymbol{\sigma}}}(\Gamma_{\hat{\boldsymbol{\sigma}}\hat{\boldsymbol{\sigma}}} + \kappa I)^{-1} \tag{22}$$

$$\boldsymbol{b}_\kappa = \bar{\boldsymbol{\sigma}} + \Gamma_{\boldsymbol{\sigma}\hat{\boldsymbol{\sigma}}}(\Gamma_{\hat{\boldsymbol{\sigma}}\hat{\boldsymbol{\sigma}}} + \kappa I)^{-1}\boldsymbol{\mu}_{\hat{\boldsymbol{\sigma}}} \tag{23}$$

allowing post-processing to be performed as a single matrix multiplication and addition, adding a minimal amount of time to processing.

V. RESULTS AND DISCUSSION

A. Comparisons from Synthetic Data

Using our Anatomical Atlas and finite element solvers described in Section III, we are able to simulate voltages for each 2-D cross-sectional conductivity distribution in the atlas. This allows us to compare performance of the original NOSER algorithm and our Mean Baby approach with and without Schur complement post-processing to ground truth conductivity distributions and assess the accuracy of each method qualitatively and quantitatively.

For qualitative comparisons we choose to look at 6 specific cases displaying different modes of pathology and visually inspect each reconstructed image comparatively to the ground truth image for structural similarities in the conductivity distributions. We note that the displays are given in the DICOM patient coordinate system, where the positive vertical axis is in the anterior direction, and right and left on the image correspond to the patient's left and right, respectively.
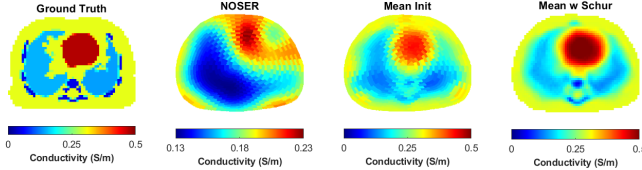

Fig. 6. Anatomically correct phantom test case and corresponding reconstructions using NOSER, the mean baby approach, and mean baby approach with Schur complement post-processing.

Our first case, seen in Figure 6 shows a typical body composition, as we can see both left and right lungs, heart as well as ribs and the spinal column. The NOSER reconstruction of this slice captures a very low conductivity right lung and high conductivity heart well, but the right lung and spinal column appear to blend together into a large "blob" and there does not appear to be any well-defined left lung. When using the Mean Baby reconstruction, we now see a clear division between the right and left lungs, as well as some definition of the spinal column. Additionally, there is a very well-defined heart in the center of the body. When applying the Schur complement post-processing to the results of the Mean Baby reconstruction, we see a further improvement to the resolution of our reconstructed image. This results in an even clearer imaging of each lung, spinal column, and heart.
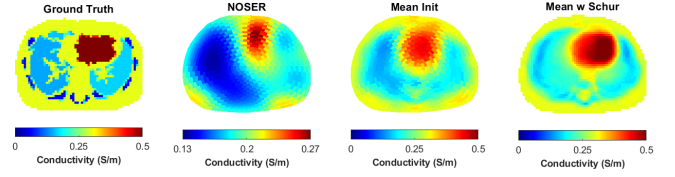

Fig. 7. Alternative phantom with both lungs present and corresponding reconstructions.

Another case with minimal pathology is shown in Figure 7; in this case we see similar results to the preceding example. The NOSER reconstruction does an improved job of identifying the presence of a left lung, but still maintains a similar presentation of the right lung and heart. The Mean Baby reconstruction once again provides an image showing both lungs, including correctly demonstrating a higher conductivity value in the left lung. In this case, however, post-processing appears to primarily blur the boundaries between lung and background tissue, possibly leaving some uncertainty in interpretation of the image in practice.
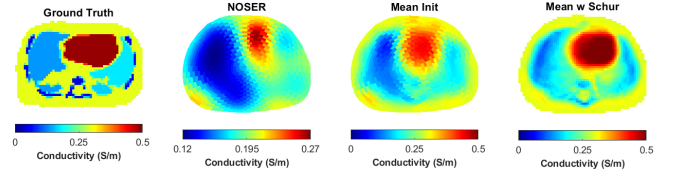

Fig. 8. Test case displaying an asymmetry where the right lung has a lower conductivity than the left lung.

Focusing on asymmetries between lungs, Figures 8 and 9, show examples of cases where both lungs are present, but the conductivity of one lung is much lower than the other. This could possibly be the result of the lung with the higher conductivity containing less air, which could be a sign of a respiratory issue in that lung. While all methods perform well in the case with a lower conductivity in the right lung, in Figure 9 we see that NOSER is not as effective at displaying a relatively higher conductivity in the left lung, in which case both lungs join together and make up a majority of the reconstructed image. Even when using the Mean Baby as an initial condition, we see there is still some difficulty in representing this specific pathology. The shapes of the lungs appear to be modeled accurately, however the conductivities between the lungs appear to be approximately equivalent. The post-processing appears to address this shortcoming adequately as the right lung appears to be less well defined than the left lung in this case.

Finally, in more drastic cases, one of the lungs may be severely compromised or even missing. We look at how each algorithm handles these cases in Figures 10 and 11. In each of these cases NOSER still appears to show the presence of both lungs, although the missing lungs are somewhat muted. Similarly, in the Mean Baby cases we still see the trace of a lower
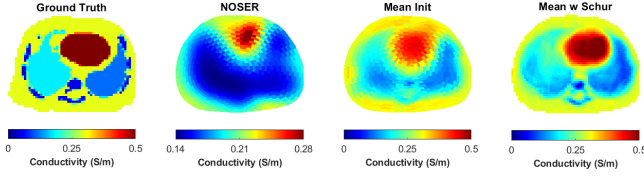
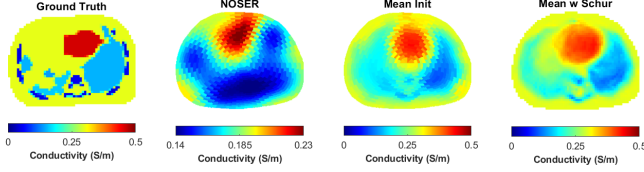Fig. 9. Asymmetrical test case with a left lung of lower conductivity than the right lung.

Fig. 10. Extreme pathological case where right lung is not present.

Case	Reconstruction	L^2 **Error**	**SSIM**	**Correlation**
Typical	NOSER	0.4825	0.4607	0.3259
	Mean Baby	0.2215	0.6101	0.8118
	Mean w Schur	0.1830	0.6906	0.8674
Both Lungs	NOSER	0.4711	0.3894	0.4273
	Mean Baby	0.2571	0.5585	0.7415
	Mean w Schur	0.1937	0.6345	0.8634
Weak Left	NOSER	0.4938	0.4019	0.4296
	Mean Baby	0.2788	0.5485	0.7276
	Mean w Schur	0.2128	0.6365	0.8398
Weak Right	NOSER	0.4890	0.3929	0.4453
	Mean Baby	0.2888	0.5750	0.7277
	Mean w Schur	0.2129	0.6816	0.8643
No Right	NOSER	0.4677	0.2793	0.4745
	Mean Baby	0.2409	0.5929	0.7048
	Mean w Schur	0.2064	0.6386	0.7777
No Left	NOSER	0.4884	0.3465	0.4723
	Mean Baby	0.2807	0.5336	0.6620
	Mean w Schur	0.1957	0.6513	0.8335

TABLE II
COMPARISON METRICS FOR EACH TEST CASE USING EACH
RECONSTRUCTION METHOD

Additionally, to assess the overall behaviors of each algorithm, the statistics were computed for each algorithm for every ground truth image in the Anatomical Atlas, with histograms shown in figure 12. A common trend appears across each of these metrics, the Mean Baby reconstruction is an improvement over the standard NOSER algorithm, while application of the Schur complement corrections resulted in further accuracy.

conductivity where the lungs are located in the mean shape itself. However, the boundaries between these values and the background tissue is blurred, which could possibly be used as an indicator that there is a more uniform conductivity than typically expected on that side of the body. The Schur complement post-processing removes most of the remaining low conductivity remnants in the lung area, and we can see the presence of the ribs are still present in the images.
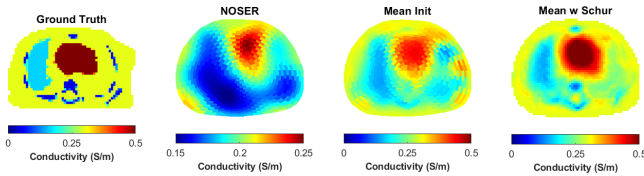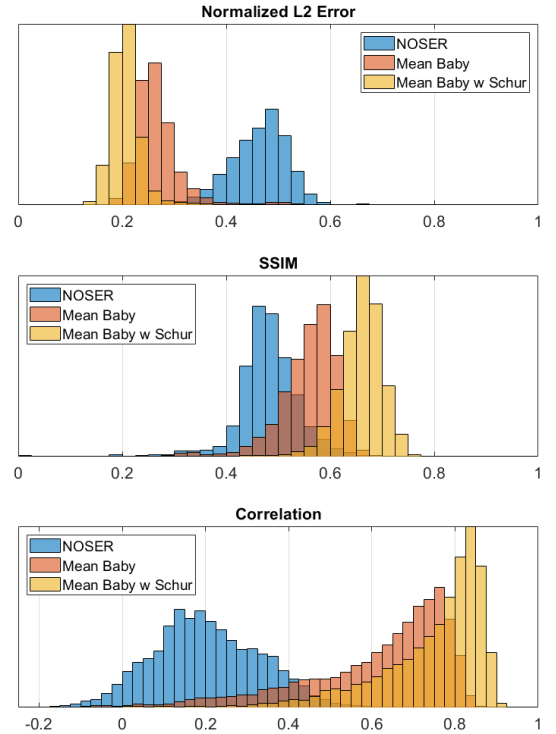

Fig. 11. Extreme pathological case where left lung is not present.

To quantitatively compare the performance of each of these reconstruction methods, we computed three metrics to measure the accuracy of each to the ground truth representation of that slice, a normalized L^2 error, structural similarity index measure (SSIM), and correlation between the images. To prioritize modeling of the inside of the body, and ensure that the reconstructed images align correctly with the ground truth data, we used the same conformal mapping of each slice that was utilized in computation of the mean baby itself as shown in 2. A table of these statistics for each of our test cases are shown in table II.

Fig. 12. Histograms of comparison statistics between reconstructions and ground truth

B. Comparisons from Clinical Data

After seeing the results using a mean initial guess and Schur complement on the Anatomical Atlas data, the next step is to test the algorithm performance on clinical data to serve as a proof of concept for the use of these algorithms in real-world scenarios. This study was conducted in accordance with the amended Declaration of Helsinki. Data were collected at Children's Hospital Colorado (CHCO) in Aurora, Colorado, under the approval of the institutional review board (IRB) (approval number 18-1843). Informed parental consent was obtained prior to participation. When considering these reconstructions there are two major points of consideration. First, since we are primarily focused on visualizing change over time, such as inflation of the lungs or beating of the heart, the primary method for visualizing EIT images in real world scenarios is through using difference imaging from a reference conductivity distribution, $\boldsymbol{\sigma}_{ref}$. That is, for each reconstructed conductivity distribution $\hat{\boldsymbol{\sigma}}_i$ for the ith frame of measurements, we display $\Delta\hat{\boldsymbol{\sigma}}_i = \hat{\boldsymbol{\sigma}}_i - \boldsymbol{\sigma}_{ref}$.
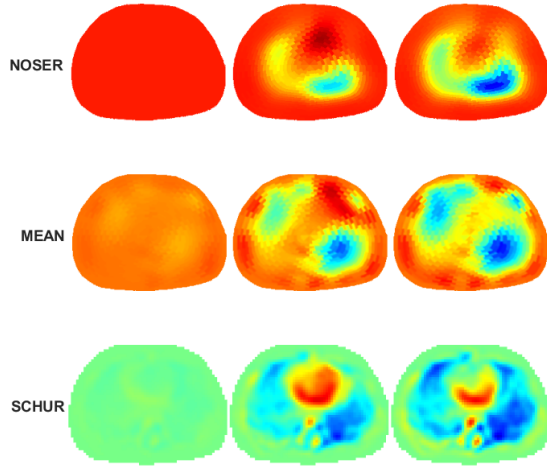

Fig. 13. Comparison of difference images of Subject 22 at full expiration, during inspiration, and full inspiration using each reconstruction algorithm

Second, these data collections were performed on live subjects at the Colorado Children's Hospital. As such, there is no ground truth for qualitative comparisons, so we are limited to qualitative comparisons between the different reconstruction images. As seen in figures 13-16, each algorithm was used to generate reconstructions using a predetermined range of measured data and reference frame. The primary focus in many of these procedures is to monitor the lungs during breathing so it is of concern to see how the reconstructions change with time as the subject breathes. We display this variation by showing 3 frames – full expiration, during inspiration, and full inspiration – for each reconstruction with reference frames chosen at expiration. We should expect to see a progression of decreasing conductivity in the lungs as air is breathed in, typically visualized as a dark blue indicating a

lower conductivity than the reference frame at each of these locations.
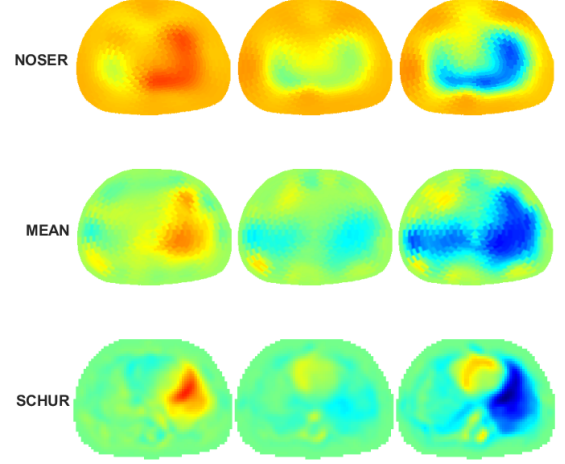

Fig. 14. Comparison of difference images of Subject 24 at full expiration, during inspiration, and full inspiration using each reconstruction algorithm

Across each of our examples we note a similar structure and progression across the different algorithms, showing that by applying the Mean Baby reconstruction the general performance of the NOSER algorithm is maintained. However, as is specifically prevalent in figures 15 and 16, NOSER has a tendency to combine the lungs into a larger "blob", where we see the Mean Baby approach creates a distinct boundary between left and right lungs more consistent with human anatomy. It may be possible in some cases, such as figure 15, to note the heart in the reconstructions at the same time. We can see in the anterior left of the NOSER reconstructions there is an area of low conductivity which appears to be more variable in the reconstructions with the mean initial case. When using the Schur complement post-processing, this variation appears to be showing as a heartbeat.

In general, however, the resulting quality upgrade of using the Schur complement is questionable. In many cases, this processing makes lung imaging much more apparent, clearly showing a boundary between the two lungs and taking on a more "lung shaped" appearance than is displayed in the other reconstructions. In cases such as Figure 16, we may see a much noisier image that blurs together multiple organs. Additionally, the Schur complement has a trend in the synthetic data to overestimate the conductivity and size of the heart, which is also evident in with the experimental data as we see notable differences in the three frames for each subject. This may mean that using the Schur complement of the experimental data may be more sensitive to the heartbeat when selecting a reference frame. Alternatively, this could also be an artifact such as how in each of the subjects shown we can note an unrealistic pulsing effect in the spinal cord.
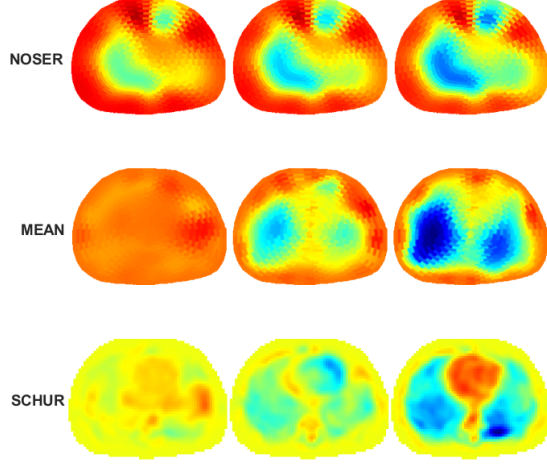
Fig. 15. Comparison of difference images of Subject 28 at full expiration, during inspiration, and full inspiration using each reconstruction algorithm
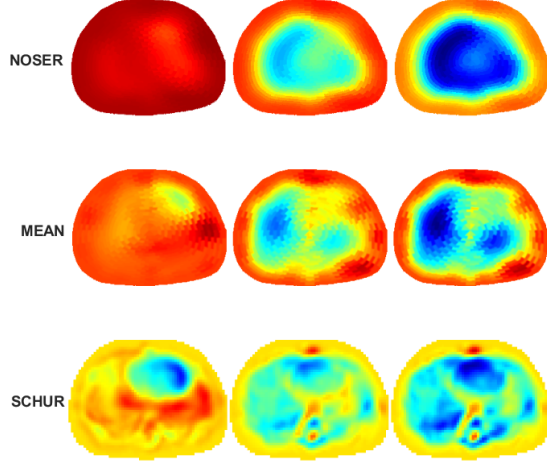

Fig. 16. Comparison of difference images of Subject 33 at full expiration, during inspiration, and full inspiration using each reconstruction algorithm

VI. CONCLUSIONS

We see that using an anatomical atlas we are able to numerically generate components to provide an anatomically informed initial guess to the NOSER algorithm. This provides a more accurate starting point for EIT reconstruction images while maintaining processing speeds for real-time imaging. Quantitatively, we see that image comparison metrics between this reconstruction to the ground truth conductivity distributions from the anatomical atlas are improved from NOSER, with further improvement when applying a Schur complement post-processing adjustment. Testing with experimentally-collected data sets qualitatively show promising improved

boundaries and clarity in difference images when compared to existing NOSER reconstructions, particularly in the identification of the lungs.

Steps ahead for implementation of this upgrade involve creation of initial condition components using expected conductivity distributions for sensing perfusion, and complex distributions to visualize the permittivity distribution in addition to conductivity. Upon which time, this can be implemented into the ACT-5[7] system to be used in real-time for patients. The success of this approach in the 16 electrode single row case for infants gives promise that a similar approach can be taken with larger patients and the 32 electrode 2 row configuration to be used with the ToDLeR[1] algorithm for creation of three-dimensional conductivity distributions. This will require an anatomical atlas of the body structure of larger patients to be used in this scenario.

REFERENCES

[1] R. BLUE, D. ISAACSON, AND J. NEWELL, *Real-time three-dimensional electrical impedance imaging*, Physiological measurement, 21 (2000), p. 15.

[2] M. CHENEY, D. ISAACSON, J. C. NEWELL, S. SIMSKE, AND J. GOBLE, *NOSER: An algorithm for solving the inverse conductivity problem*, International Journal of Imaging systems and technology, 2 (1990), pp. 66–75.

[3] H. EDGAR, S. DANESHVARI BERRY, E. MOES, N. ADOLPHI, P. BRIDGES, AND K. NOLTE, *New mexico decedent image database*, 2020.

[4] K. HOWARD, C. ROCHELEAU, T. OVERTON, J. BARRAZA NAVA, M. FALDET, K. MOEN, S. SOLLER, T. STEPHENS, E. VAN DE LAGEMAAT, N. WIJESINGHE, K. WONG DOLLOFF, N. BARBOSA DE ROSA, AND J. MUELLER, *A comparison of techniques to improve pulmonary eit image resolution using a database of simulated eit images [manuscript submitted for publication]*, Journal of Computational and Applied Mathematics, (2024).

[5] T. B. R. SANTOS, R. M. NAKANISHI, E. D. L. B. DE CAMARGO, M. B. P. AMATO, J. P. KAIPIO, R. G. LIMA, AND J. L. MUELLER, *Improved resolution of d-bar images of ventilation using a schur complement property and an anatomical atlas*, Medical Physics, (2022).

[6] T. B. R. SANTOS, R. M. NAKANISHI, J. P. KAIPIO, J. L. MUELLER, AND R. G. LIMA, *Introduction of sample based prior into the d-bar method through a schur complement property*, IEEE transactions on medical imaging, 39 (2020), pp. 4085–4093.

[7] O. R. SHISHVAN, A. ABDELWAHAB, N. BARBOSA DA ROSA, G. J. SAULNIER, J. L. MUELLER, J. C. NEWELL, AND D. ISAACSON, *ACT5 electrical impedance tomography system*, IEEE Transactions on Biomedical Engineering, (2023), pp. 1–10.

[8] E. SOMERSALO, M. CHENEY, AND D. ISAACSON, *Existence and uniqueness for electrode models for electric current computed tomography*, SIAM Journal on Applied Mathematics, 52 (1992), pp. 1023–1040.

[9] THE MATHWORKS INC., *MATLAB version: 9.14.0 (R2023a)*, 2023.

[10] P. YUSHKEVICH, J. PIVEN, H. HAZLETT, R. SMITH, S. HO, J. GEE, AND G. GERIG, *User-guided 3d active contour segmentation of anatomical structures: Significantly improved efficiency and reliability*, NeuroImage, (2006).